

# Identification of Hydrogen Bonds Using Quantum Electrodynamics

Masato Senami\* and Keito Ito

*Department of Micro Engineering, Kyoto University, Kyoto 615-8540, Japan*

(Dated: June 19, 2020)

## Abstract

A method for the identification of hydrogen bonds was investigated from the viewpoint of the stress tensor density proposed by Tachibana and following other works in this field. Hydrogen bonds are known to exhibit common features with the ionic and covalent bonds. In quantum electrodynamics, the covalent bond has been demonstrated to display a spindle structure of the stress tensor density. Importantly, this spindle structure is also seen in the hydrogen bond, although the covalency is considerably weaker than in a typical covalent bond. The discrimination from the ionic bond is the most imperative for the identification of the hydrogen bond. In the present study, the directionality of the hydrogen bond is investigated, as the ionic bond is nearly isotropic, while the hydrogen bond exhibits the directionality. It was demonstrated that the hydrogen bond can be discriminated from the ionic bond by the angle dependence of the largest eigenvalue of the stress tensor density.

---

\*Electronic address: [senami@me.kyoto-u.ac.jp](mailto:senami@me.kyoto-u.ac.jp)

## I. INTRODUCTION

Chemical bonds have been actively investigated from the viewpoint of the quantum theory since Heitler and London, which involved evaluation of chemical bonds based on quantum mechanics[1–3]. Specifically, topological analyses of wave-functions, such as the quantum theory of atoms in molecules (QTAIM) [4, 5] and the topology of the electron localization function (ELF) [6], have attracted considerable attention. Based on these evaluations, a chemical bond can be classified as covalent or ionic using topological parameters, such as  $\nabla\rho$ , where  $\rho$  denotes the electron density. The aforementioned real space analyses are relatively novel trends employed for the investigation of chemical bonds [7–9], particularly the hydrogen bond [10].

Our group and coworkers have recently developed a real space analysis method using stress tensor density, which was originally proposed by Tachibana and is a new density quantity based on quantum electrodynamics (QED) [11]. The approach offers a new platform for gaining a better understanding of chemical bonds. Notably, the classification of chemical bonds has been previously carried out utilizing the stress tensor density [12–15]. Previous studies included the identification of the covalent, metallic, and ionic bonds [16–19]. The bond order based on QED was particularly well established for covalent bonds and shows an excellent correlation with the internuclear distances of numerous chemical bonds [16, 20]. The bond orders of other bonds are currently being investigated and will undoubtedly be reported in the near future.

In the present work, we extend the scope of real space analysis utilizing the stress tensor to identify the hydrogen bond. The identification of ionic bonds is also confirmed using models involving periodic boundary conditions, as the previous studies concerning the ionic bond employed cluster models [19]. Since hydrogen bonds exhibit analogous distribution patterns of the stress tensor density to those of ionic bonds as shown later, the establishment of ionic bond features is necessary. Moreover, hydrogen bonds are formed by electrostatic interactions between hydrogen atoms and acceptor atoms displaying large electronegativities; thus, they are considered to exhibit similar features to ionic bonds. In addition to the ionicity, hydrogen bonds are also known to have comparable features to covalent bonds [21]. Ionic bonds exhibit isotropic features, while the covalency of hydrogen bonds results in directionality. Thus, to discriminate from ionic bonds, particular attention was paid to the

directionality of the investigated bonds. Our analysis in the present paper is a non-scalar and directional one.

This present paper is organized as follows. In the first section, the quantities based on QED are reviewed and the method for identification of chemical bonds is summarized. In the following section, the details concerning the performed computations are elucidated. The dependence of our approach on computational methods, such as Hartree-Fock and density functional theory (DFT), is also discussed. In the fourth section, the method for identification of hydrogen bonds is described from the viewpoint of real space analysis. The approach for the identification of ionic bonds is confirmed utilizing models involving periodic boundary conditions. For hydrogen bonds, the stress tensor density, differential eigenvalues of this tensor, and the kinetic energy density are determined and compared with other bonds, i.e., the covalent, metallic, and ionic bonds. The penultimate section evaluates the directionality of the distribution of the stress tensor density of hydrogen bonds to discriminate them from ionic bonds. Finally, the last section presents the summary and our conclusions.

## II. THEORY

In this section, the quantities defined by our group and others are introduced. Detailed explanations of these QED quantities can be found in the available literature [11, 14, 15]. In relativistic quantum theory, an electron is described as the four-component Dirac field, whereas the photon is defined as the U(1) gauge vector field. Moreover, the electron field is denoted by  $\hat{\Psi}(x)$  while the photon field is denoted by  $\hat{A}(x)$ . For the gauge field, the Coulomb gauge condition,  $\vec{\nabla} \cdot \hat{A}(x) = 0$ , is adopted for the gauge fixing. The space-time coordinate is described by  $x = (ct, \vec{r})$ . The Einstein summation convention is assumed, and Greek (Latin) indices run over 0 to 3 (1 to 3).

The operator of the electronic kinetic momentum density is defined as:

$$\hat{\Pi}_e(x) = \frac{1}{2} \left[ i\hbar \hat{\Psi}^\dagger(x) \hat{D}_e(x) \hat{\Psi}(x) - i\hbar \left( \hat{D}_e(x) \hat{\Psi}(x) \right)^\dagger \hat{\Psi}(x) \right], \quad (1)$$

where  $\hbar$  is the reduced Planck constant, and the Hermitian conjugate is denoted by the superscript dagger,  $\dagger$ . The Dirac conjugate is defined as  $\hat{\bar{\psi}} \equiv \hat{\psi}^\dagger(x) \gamma^0$ , where  $\gamma^\mu$  ( $\mu = 0 - 3$ ) is the gamma matrix. The covariant derivative is given by  $\hat{D}_{ek} = \partial_k + i \frac{Z_e e}{\hbar c} \hat{A}_k(x)$ , where  $e$  is

the elementary charge, ( $e > 0$ ).  $Z_e = -1$  indicates the charge of the electron, and  $c$  is the speed of light in vacuum.

The time derivative of  $\hat{\Pi}_e(x)$  is given by the sum of the Lorentz force density operator,  $\hat{\vec{L}}_e(x)$ , and the electronic tension density operator,  $\hat{\tau}_e^{\Pi k}(x)$ , according to the following equation:

$$\frac{\partial}{\partial t} \hat{\Pi}_e(x) = \hat{\vec{L}}_e(x) + \hat{\tau}_e^{\Pi}(x). \quad (2)$$

The Lorentz force density operator is defined as:

$$\hat{\vec{L}}_e(x) = \hat{\vec{E}}(x) \hat{\rho}_e(x) + \frac{1}{c} \hat{\vec{j}}_e \times \hat{\vec{B}}(x), \quad (3)$$

where  $\hat{\rho}_e(x)$  is the electronic charge density operator,  $\hat{\vec{j}}_e(x)$  is the electronic charge current density operator,  $\hat{\vec{E}}(x)$  is the electric field density operator, and  $\hat{\vec{B}}(x)$  is the magnetic field density operator. Additionally, the electronic tension density operator is defined by the following equation:

$$\begin{aligned} \hat{\tau}_e^{\Pi k}(x) = & \frac{i\hbar c}{2} \left[ \left( \hat{D}_{el}(x) \hat{\Psi}(x) \right)^\dagger \gamma^0 \gamma^l \hat{D}_{ek}(x) \hat{\Psi}(x) + \hat{\Psi}(x) \gamma^l \hat{D}_{ek}(x) \hat{D}_{el}(x) \hat{\Psi}(x) \right. \\ & - \left( \hat{D}_{ek}(x) \hat{D}_{el}(x) \hat{\Psi}(x) \right)^\dagger \gamma^0 \gamma^l \hat{\Psi}(x) - \left( \hat{D}_{ek}(x) \hat{\Psi}(x) \right)^\dagger \gamma^0 \gamma^l \hat{D}_{el}(x) \hat{\Psi}(x) \left. \right] \\ & - \frac{1}{c} \left( \hat{\vec{j}}_e(x) \times \hat{\vec{B}}(x) \right)^k. \end{aligned} \quad (4)$$

The electronic tension density operator is also given as the divergence of the electronic stress tensor density operator,  $\hat{\tau}_e^{\Pi kl}(x)$ :

$$\hat{\tau}_e^{\Pi k}(x) = \partial_l \hat{\tau}_e^{\Pi kl}(x). \quad (5)$$

It is noteworthy that some ambiguity exists in the definition of the electronic stress tensor density operator, as any term can be added when the divergence of the term is zero. Thus, we adopt the following definition of the electronic stress tensor density operator:

$$\hat{\tau}_e^{\Pi kl}(x) = \frac{i\hbar c}{2} \left[ \hat{\psi}(x) \gamma^l \hat{D}_{ek}(x) \hat{\psi}(x) - \left( \hat{D}_{ek}(x) \hat{\psi}(x) \right)^\dagger \gamma^0 \gamma^l \hat{\psi}(x) \right], \quad (6)$$

from the viewpoints of the Lorentz covariance, gauge symmetry, and hermiticity.

In the present work, the target molecules consist only of light elements and relativistic effects are negligible. Consequently, we employed nonrelativistic treatment of these quantities

[22, 23]. In this approximation, the small components in the four-component spinor in the Dirac representation are replaced by large components according to the following equation:

$$\hat{\psi}_S(x) \simeq -\frac{1}{2mc} i\hbar \sigma^k \hat{D}_{ek}(x) \hat{\psi}_L(x) \quad (7)$$

where  $m$  denotes the electron mass. In this approximation, some spin-dependent terms are excluded. Taking the above into consideration, Eq. (2) can be reduced to the nonrelativistic form, as per following equation:

$$\frac{\partial}{\partial t} \left( m \hat{v}_e(x) \right) = \hat{L}_e(x) + \hat{\tau}_e^S(x), \quad (8)$$

where  $\hat{v}_e(x)$  is the velocity density operator,  $\hat{\Pi}(x) \approx m \hat{v}_e(x)$ , and  $\hat{\tau}_e^S(x)$  is the nonrelativistic representation of the tension density operator, which is given by:

$$\begin{aligned} \hat{\tau}_e^{Sk}(x) &= \frac{\hbar^2}{4m} \left[ \hat{\psi}_L^\dagger(x) \hat{D}_{ek}(x) \hat{D}_e^2(x) \hat{\psi}_L(x) + \left( \hat{D}_{ek}(x) \hat{D}_e^2(x) \hat{\psi}_L(x) \right)^\dagger \hat{\psi}_L(x) \right. \\ &\quad \left. - \left( \hat{D}_{ek}(x) \hat{\psi}_L(x) \right)^\dagger \hat{D}_e^2(x) \hat{\psi}_L(x) - \left( \hat{D}_e^2(x) \hat{\psi}_L(x) \right)^\dagger \hat{D}_{ek}(x) \hat{\psi}_L(x) \right] \\ &\quad - \frac{1}{c} \left( \vec{j}_e(x) \times \vec{B}(x) \right)^k \\ &= \partial_l \hat{\tau}_e^{Skl}(x). \end{aligned} \quad (9)$$

Here,  $\hat{\tau}_e^{Skl}(x)$  is the nonrelativistic representation of the electronic stress tensor density operator, which is given by:

$$\begin{aligned} \hat{\tau}_e^{Skl}(x) &= \frac{\hbar^2}{4m} \left[ \hat{\psi}_L(x) \hat{D}_{ek}(x) \hat{D}_{el}(x) \hat{\psi}_L(x) + \left( \hat{D}_{ek}(x) \hat{D}_{el}(x) \hat{\psi}_L(x) \right)^\dagger \hat{\psi}_L(x) \right. \\ &\quad \left. - \left( \hat{D}_{ek}(x) \hat{\psi}_L(x) \right)^\dagger \hat{D}_{el}(x) \hat{\psi}_L(x) - \left( \hat{D}_{el}(x) \hat{\psi}_L(x) \right)^\dagger \hat{D}_{ek}(x) \hat{\psi}_L(x) \right]. \end{aligned} \quad (10)$$

Pauli formulated firstly this nonrelativistic form of the stress tensor based on the basic idea by Schrödinger. Then, the nonrelativistic stress tensor was developed by Epstein in his virial theory [24] and Bader in QTAIM [4]. The nonrelativistic form of the tension density is also discussed as Ehrenfest force [25] in QTAIM.

In an equilibrium system, on average, electrons in the system should not receive any acceleration and deceleration; hence, the expectation value of Eq. (8) can be expressed as:

$$0 = \langle \hat{L}_e^k(x) \rangle + \langle \hat{\tau}_e^{Sk}(x) \rangle. \quad (11)$$

This means that in equilibrium states, the Lorentz force density and the tension density should cancel out. The tension density is the counter force to the Lorentz force density in

equilibrium states. It has been previously confirmed numerically that in electronic structure computations, where systems are in equilibrium, this cancellation does occur [26]. Furthermore, with the existence of the tension density, distributions of electrons in atoms and molecules do not shrink into nuclei in quantum field theory.

For simplicity, in the following considerations, the expectation value of operators are denoted by characters without the hat symbol,  $\hat{\phantom{x}}$ , and the bra-ket notation,  $\langle \phantom{x} \rangle$ . For example,  $\tau_e^{Sk}(\vec{r})$  and  $\tau_e^{Sk}(\vec{r})$  indicate  $\langle \hat{\tau}_e^{Sk}(x) \rangle$  and  $\langle \hat{\tau}_e^{Sk}(x) \rangle$ , respectively. In practical computations, quantum field theory electronic structures are not available yet, with the exception of certain corrections, such as the Bethe-Salpeter equation. Thus, the expectation values of these equations can be calculated by substituting the wave functions computed using quantum mechanics. Moreover, the vector potential is excluded, since its effect on the electronic structure computed in quantum mechanics is negligible [27]. By this elimination, our wave functions were derived based on quantum mechanics. Nevertheless, the use of the formulation based on QED sheds light on the understanding of atoms and molecules. With this substitution,  $\tau_e^{Sk}(\vec{r})$  and  $\tau_e^{Sk}(\vec{r})$  can be given as:

$$\tau_e^{Sk}(\vec{r}) = \frac{\hbar^2}{4m} \sum_i \nu_i \left[ \psi_i^\dagger(\vec{r}) \frac{\partial \Delta \psi_i(\vec{r})}{\partial x^k} - \frac{\partial \psi_i^\dagger(\vec{r})}{\partial x^k} \Delta \psi_i(\vec{r}) + \frac{\partial \Delta \psi_i^\dagger(\vec{r})}{\partial x^k} \psi_i(\vec{r}) - \Delta \psi_i^\dagger(\vec{r}) \frac{\partial \psi_i(\vec{r})}{\partial x^k} \right], \quad (12)$$

$$\tau_e^{Sk}(\vec{r}) = \frac{\hbar^2}{4m} \sum_i \nu_i \left[ \psi_i^\dagger(\vec{r}) \frac{\partial^2 \psi_i(\vec{r})}{\partial x^k \partial x^l} - \frac{\partial \psi_i^\dagger(\vec{r})}{\partial x^k} \frac{\partial \psi_i(\vec{r})}{\partial x^l} + \frac{\partial^2 \psi_i^\dagger(\vec{r})}{\partial x^k \partial x^l} \psi_i(\vec{r}) - \frac{\partial \psi_i^\dagger(\vec{r})}{\partial x^l} \frac{\partial \psi_i(\vec{r})}{\partial x^k} \right], \quad (13)$$

where  $\psi_i(\vec{r})$  is the  $i$ -th natural orbital,  $\nu_i$  is its occupation number, and  $\Delta \equiv \sum_{k=1}^3 (\partial/\partial x^k)^2$  is the Laplacian.

It has been demonstrated that a chemical bond can be classified by these quantities, as explained in more detail below [16, 17, 19, 28]. Before the explanation of this classification, some additional quantities and notions used in the identification of other types of chemical bonds must be introduced.

The stress tensor density is a  $3 \times 3$  matrix defined at any position. This tensor can be

diagonalized as:

$$\overset{\leftrightarrow}{\tau}_e^S(\vec{r}) = \begin{pmatrix} \tau_{e\,xx}^S(\vec{r}) & \tau_{e\,xy}^S(\vec{r}) & \tau_{e\,xz}^S(\vec{r}) \\ \tau_{e\,yx}^S(\vec{r}) & \tau_{e\,yy}^S(\vec{r}) & \tau_{e\,yz}^S(\vec{r}) \\ \tau_{e\,zx}^S(\vec{r}) & \tau_{e\,zy}^S(\vec{r}) & \tau_{e\,zz}^S(\vec{r}) \end{pmatrix} \xrightarrow{\text{diagonalize}} \begin{pmatrix} \tau_e^{S11}(\vec{r}) & 0 & 0 \\ 0 & \tau_e^{S22}(\vec{r}) & 0 \\ 0 & 0 & \tau_e^{S33}(\vec{r}) \end{pmatrix}. \quad (14)$$

In the present work, we adopted  $\tau_e^{S33}(\vec{r}) \geq \tau_e^{S22}(\vec{r}) \geq \tau_e^{S11}(\vec{r})$ . The principal stress and its principal axis are identified following diagonalization. The positive principal stress is also called the tensile stress, while the negative stress can be denoted as compressive stress. The energy density is represented by three eigenvalues of the stress tensor:

$$\varepsilon_\tau^S(\vec{r}) = \frac{1}{2} \sum_{k=1}^3 \tau_e^{Skk}. \quad (15)$$

The virial theorem is employed in this derivation. The total electronic energy of the system is equal to the integrated value of this energy density over the whole space. The energy density at the Lagrange point defines the bond order based on QED, which parametrizes the strength of the covalent bond. The Lagrange point,  $\vec{r}_L$ , is defined as the point where the tension density,  $\tau_e^{Sk}(\vec{r})$ , between two nuclei, equals zero, i.e.,  $\tau_e^{Sk}(\vec{r}_L) = 0$ . The bond order is defined by the following equation:

$$b_\varepsilon = \frac{\varepsilon_{\tau\text{AB}}^S(\vec{r}_L)}{\varepsilon_{\tau\text{HH}}^S(\vec{r}_L)}. \quad (16)$$

The bond order of a chemical bond between atoms A and B is expressed as the ratio of the energy density at the Lagrange point between atoms A and B and the energy density at the Lagrange point between two hydrogen atoms of a  $\text{H}_2$  molecule. In this case, the energy density of a  $\text{H}_2$  molecule should be calculated using the same computational conditions, such as the basis set.

The kinetic energy density operator is defined by the following equation:

$$\hat{T}_e(x) = -\frac{\hbar^2}{2m} \frac{1}{2} \left[ \hat{\psi}^\dagger(x) \hat{D}_e^2(x) \hat{\psi}(x) + \left( \hat{D}_e^2(x) \hat{\psi}(x) \right)^\dagger \hat{\psi}(x) \right], \quad (17)$$

and the expectation value of this operator is given by:

$$n_{T_e}(\vec{r}) = -\frac{\hbar^2}{4m} \sum_i \nu_i \left[ \psi_i^\dagger(\vec{r}) \Delta \psi_i(\vec{r}) + \left( \Delta \psi_i^\dagger(\vec{r}) \right) \psi_i(\vec{r}) \right]. \quad (18)$$

Additionally the surface of an atom or a molecule is defined as the surface of  $n_{T_e}(\vec{r}) = 0$ , which denotes the electronic interface. The region of  $n_{T_e}(\vec{r}) > 0$  is called the electronic drop

region ( $R_D$ ), where the electron is considered to move with positive energy. Conversely, the region of  $n_{T_e}(\vec{r}) < 0$  is the electronic atmosphere region ( $R_A$ ), where the electron exists as a quantum phenomenon.

Lastly, the classification of a chemical bond by these quantities is explained. The covalent bond can be identified by the spindle structure formed by the largest eigenvalue and eigenvector of the stress tensor density [28]. The largest eigenvalue has a positive value around the Lagrange point and the eigenvector connects two atoms in the shape of a spindle. Furthermore, the electronic drop region contains two atoms forming a covalent bond. The metallic bond can be identified based on the degeneracy of the three eigenvalues of the stress tensor density at the Lagrange point between two atoms participating in such a bond [17]. Generally, positive eigenvalues are not seen in condensed matter forming a metallic bond. All atoms are contained in a single electronic drop region. The ionic bond has been determined to have separate ionic surfaces defined by the electronic interface, in addition to the charge transfer between two atoms forming the bond [19]. This shape of the electronic interface implies that the bonding between the cations and anions involves electrostatic interactions. The largest eigenvalue is positive around the surface of cations, while both largest positive and negative eigenvalues are observed around the surface of anions. For instance, anions of fluorine and oxygen have often positive values, while anions of heavier elements such as chlorine typically exhibit negative values. Thus, for ionic bonds, the largest eigenvalue is frequently positive around the Lagrange point. Because of this feature, if a chemical bond has weak covalency in addition to ionicity, it is challenging to find the covalent properties. As demonstrated below, this is also the case for hydrogen bonds, and thus, the present work attempts to investigate the identification of the covalency properties in the presence of large electrostatic forces.

### III. COMPUTATIONAL DETAIL

In this section, the computational aspects of our study are explained in detail. The atomic unit is used throughout unless stated otherwise.



## A. Ionic bond

In the first instance, the computation to confirm the identification of ionic bonds was performed for models with periodic boundary conditions. In the previous work [19], cluster models were utilized to study the properties of ionic bonds. Although the reported models were sufficiently large, in the present work, the properties identifying ionic bonds were confirmed with the periodic boundary conditions.

For this purpose, typical ionic crystals, i.e., LiF, LiCl, NaF, and NaCl, were studied. The rock-salt crystal structure was adopted in the models, and the chosen lattice parameters were identical to the ones reported previously [19]. The OpenMX program package [29, 30] was employed for the electronic structure computations with periodic boundary conditions. This program package is based on DFT, norm-conserving pseudo-potentials, and pseudo-atomic localized basis functions. The local spin density approximation functional of Ceperley-Alder [31] was used in our computations. For the basis sets, we chose Li10.0-s2p1d1 and F6.0-s1p1 for LiF, Li10.0-s3p2d1 and Cl7.0-s2p1d1 for LiCl, Na9.0-s3p2d1f1 and F6.0-s2p1 for NaF, and Na9.0-s3p2d1f1 and Cl7.0-s2p2d1 for NaCl. The  $4 \times 4 \times 4$   $k$ -point mesh was adopted and the temperature of electrons was set at 300 K. Several physical quantities explained in the previous section were calculated for the electronic structures derived by these computations. The computations of the physical quantities of QED were carried out by the program package, QEDynamics [32].

## B. Hydrogen bond

Cluster models consisting of two molecules were used for the evaluation of hydrogen bonds. In addition, computations with the molecular orbital method were employed in the study. Electronic structure computations were carried out by Gaussian 09 program package [33]. The coupled-cluster method restricted to single and double excitation (CCSD) was adopted, and the aug-cc-pVTZ basis set [34] was used for all atoms. The performed geometric optimization computations included the counterpoise correction for the basis set superposition error.

Six models shown in Fig. 1 were used for the study of hydrogen bonds. The models were composed of HF, H<sub>2</sub>O, and NH<sub>3</sub>, which are typical molecules forming hydrogen bonds.

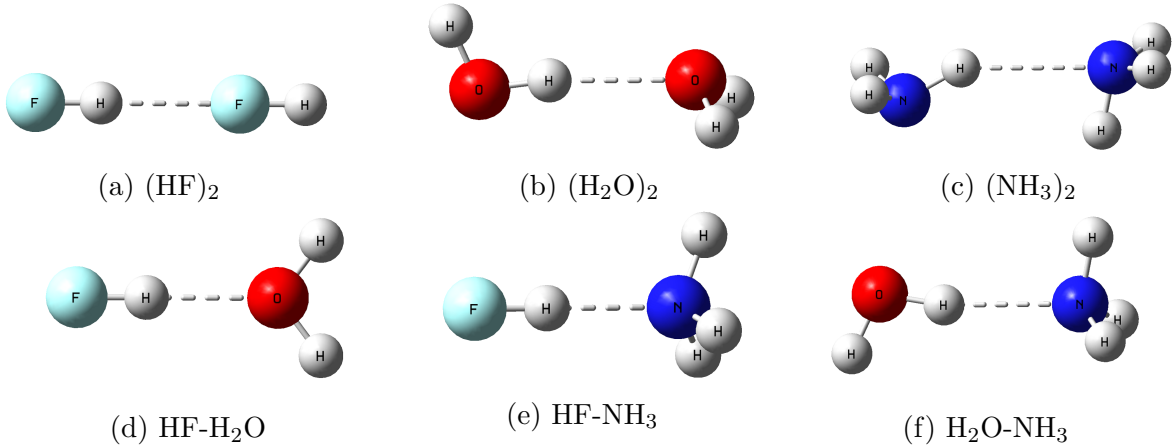


FIG. 1: Models for the study of hydrogen bond.

It is noteworthy that three models involved homodimers, which are  $(\text{HF})_2$ ,  $(\text{H}_2\text{O})_2$ , and  $(\text{NH}_3)_2$ , and the remaining three considered heterodimers, which are  $\text{HF}-\text{H}_2\text{O}$ ,  $\text{HF}-\text{NH}_3$  and  $\text{H}_2\text{O}-\text{NH}_3$ .

Some other cluster models are also employed for the comparison with ionic, metallic, and covalent bonds.  $\text{LiF}$  and  $\text{NaCl}$  are used as examples of clusters containing ionic bonds. For models of typical metallic and covalent bonds,  $\text{Li}$  and diamond clusters are adopted, respectively. The structure and computational details chosen in the present study are identical to those previously reported [19]. For the computations of physical quantities of QED, QEDynamics [32] was utilized for the electronic structures derived using Gaussian 09.

### C. Dependence of the computational method

In this section, the differences in the QED quantities determined using various computational methods are evaluated. The model composed of two hydrogen fluoride molecules,  $(\text{HF})_2$ , was employed for the study. We compared the outcomes of Hartree-Fock (HF), DFT with the B3LYP and PBE0 functionals, second-order Møller Plesset (MP2), and CCSD analyses.

The eigenvalues of the stress tensor at the Lagrange point as well as the internuclear length of the hydrogen bond of  $(\text{HF})_2$  are shown in Table I. The internuclear length was derived by geometric optimization computations explained in the above sections. The result of CCSD is considered to be the most reliable. The remaining values of the internuclear lengths vary by approx. 5%. On the other hand, the eigenvalues of the stress tensor are

TABLE I: The eigenvalues of the stress tensor at the Lagrange point and the internuclear length of the hydrogen bond of (HF)<sub>2</sub>. The results of Hartree-Fock (HF), DFT with the B3LYP and PBE0 functionals, MP2, and CCSD are shown. The value of 1 [a.u.] of the stress tensor is  $2.94210 \times 10^{13}$  N/m<sup>2</sup> in the SI units.

Method	Internuclear length [Å]	$\tau_e^{S33}$ [a.u.]	$\tau_e^{S22}$ [a.u.]	$\tau_e^{S11}$ [a.u.]
HF	2.0057	$1.8020 \times 10^{-3}$	$-8.6771 \times 10^{-3}$	$-8.6771 \times 10^{-3}$
B3LYP	1.9048	$3.4464 \times 10^{-3}$	$-1.2007 \times 10^{-2}$	$-1.2007 \times 10^{-2}$
PBE0	1.9034	$3.3848 \times 10^{-3}$	$-1.1854 \times 10^{-2}$	$-1.1854 \times 10^{-2}$
MP2	1.9396	$2.0076 \times 10^{-3}$	$-1.0021 \times 10^{-2}$	$-1.0021 \times 10^{-2}$
CCSD	1.9473	$1.9195 \times 10^{-3}$	$-1.0254 \times 10^{-2}$	$-1.0254 \times 10^{-2}$

strongly dependent on the choice of the computational method. The results obtained by DFT and HF are deviated from that determined by CCSD are approx. 15-20% for  $\tau_e^{S22}$  and  $\tau_e^{S11}$ , where these two parameters have the same value due to the axial symmetry of the structure. Notably, the largest eigenvalues obtained by DFT are nearly two-fold higher than the CCSD value. Based on these outcomes, MP2 and CCSD are considered to be optimal. The results determined utilizing these two computational methods are within 5%. Although the value of  $\tau_e^{S33}$  is significantly different between DFT and CCSD, the distribution pattern of the largest eigenvalue and its eigenvectors maintains good similarity for the identification of chemical bonds as shown in Fig. 2. The electronic interface of the two molecules is clearly separate and the spindle structure between the two atoms (the hydrogen nucleus at  $x \sim -0.7$  Å and the fluorine nucleus at  $x \sim 1.2$  Å) is apparently formed, although a different pattern is observed around the right fluorine atom. CCSD and MP2 are appropriate choices for computations, while DFT and HF computations have been determined as sufficient for the classification of chemical bonds. In the present work, however, the CCSD method was adopted based on the accuracy of the eigenvalues, in addition to the distribution pattern.

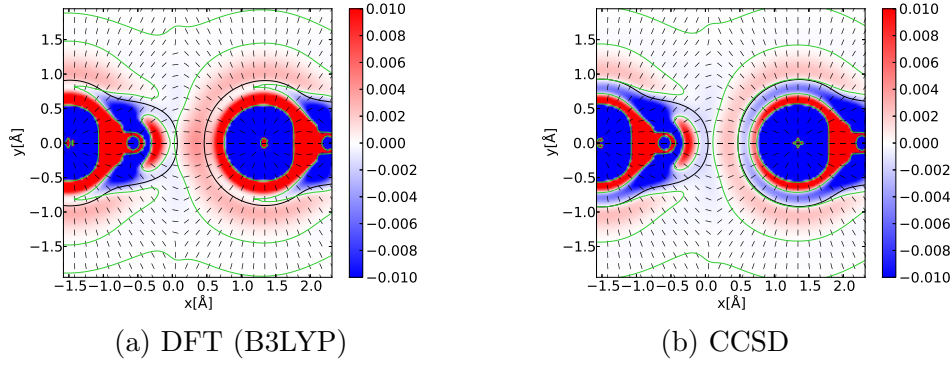


FIG. 2: The distribution pattern of the largest eigenvalue and its eigenvectors for  $(\text{HF})_2$ . The colors indicate the value of the eigenvalue, and the blue and red regions denote negative and positive values, respectively. The value is zero on the green solid lines. Black line segments represent the directions of the eigenvectors. Black solid line demonstrates the electronic interface, where the kinetic energy density is zero.

## IV. RESULTS

### A. Confirmation of the classification of the ionic bond

In this subsection, the properties of ionic bonds were confirmed by models with periodic boundary conditions. The summary of the properties involved separate ionic surfaces and the charge transfer between donors and acceptors. The models described herein include sufficient charge transfer; therefore, in the present section, only the former is evaluated. Subsequently, we also examined the distribution to the largest eigenvalue of the stress tensor for comparison.

The distribution of the kinetic energy density of ionic crystals is shown in Fig. 3. Panels (a), (b), (c), and (d) correspond to the results obtained for LiF, LiCl, NaF, and NaCl, respectively. The positive kinetic energy density values are indicated in yellow, while the negative ones are shown in blue. The black solid lines denote the contour of zero kinetic energy density. This contour is drawn by using the data filtered by the Gaussian filter, since the distribution of the kinetic energy density contains some noisy patterns around the electronic interface, which is the surface of the zero kinetic energy density. The kinetic energy density itself is depicted by the unfiltered data. It can be seen that the electronic interface is evidently separate for anions and cations. Thus, it can be confirmed that the ionic bond

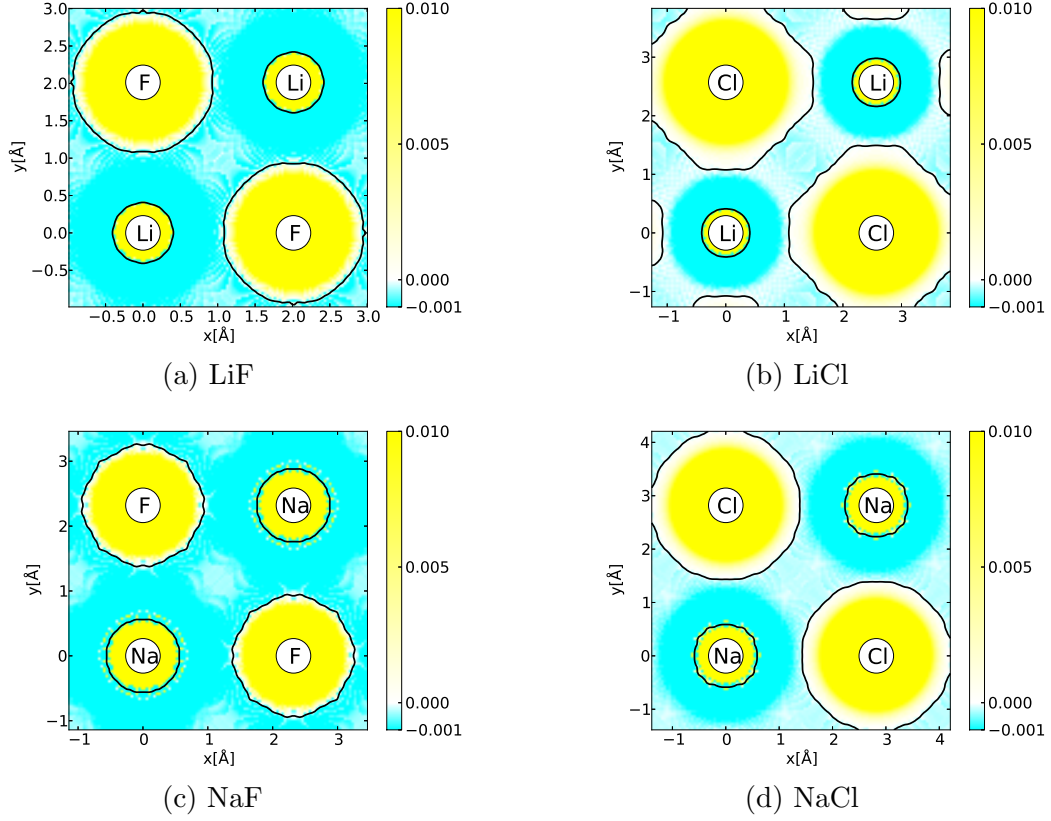


FIG. 3: The distribution of the kinetic energy density of ionic crystals. The positive kinetic energy density values are marked in yellow, while the negative ones are shown as blue regions. Black solid lines indicate kinetic energy density equal to zero. The contour is based on the filtered data.

identification method reported previously [19] is valid for models with periodic boundary conditions, which represent condensed matter. In addition, the area of the electronic drop region (positive kinetic energy density region) around the anion is considerably larger than that of the cation. Because the cation transfers an electron to the anion, the screening effect on the valence electrons is weakened and the radius of the electronic drop region is shrunken.

The distribution of the largest eigenvalue and its eigenvector of the stress tensor are shown in Fig. 4. Green solid lines indicate the surface where the largest eigenvalue of the stress tensor density is zero, while the black lines denote the kinetic energy density equal to zero. Similarly to Fig. 3, the contours were obtained using the filtered data. Black line segments represent the direction of the eigenvector corresponding to the largest eigenvalue. The distributions of the largest eigenvalue and eigenvector confirm that the models with periodic boundary conditions and the cluster models are in good agreement. As mentioned

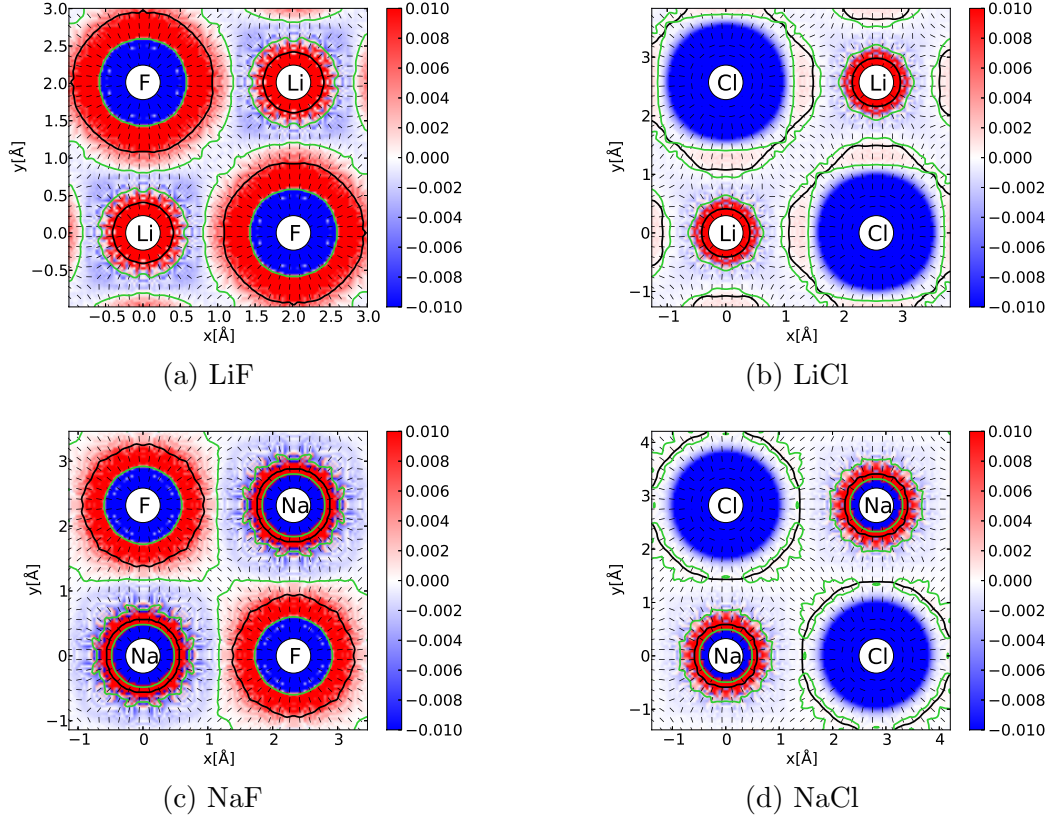


FIG. 4: The distribution of the largest eigenvalue and its eigenvector of the stress tensor. The eigenvalue is the zero on green solid lines. Black line segments represent the direction of the eigenvector. Black solid lines show the electronic interface, where the kinetic energy density is zero. These contours are based on the filtered data.

above, results of the cluster models have been previously reported [19] and in the present work are presented in Fig. 9. It should be noted that OpenMX uses pseudopotential for the inner core electrons and hence the difference around the nuclei is not significant. Thus, the cluster models can be effectively employed to identify ionic bonds. The directions of the eigenvectors around all nuclei exhibit a radial pattern and it may be considered that the eigenvectors connect nearby atoms. The absence of degeneracy between three eigenvalues of the stress tensor may lead to incorrect speculation that this bond has directionality. Since the radial pattern of the eigenvector is nearly isotropic, the considered bond does not have any directionality, which is plausible for an ionic bond. The largest eigenvalue often displays a positive value around the electronic interface, which makes finding the covalency hidden in an ionic bond challenging. This is however the key to the identification of hydrogen bonds.

Finally, we will discuss the Gaussian filter, which was used for the computations of the

stress tensor density and the kinetic energy density contours. This filter is used only in the current subsection and only for the wave function derived by OpenMX. It can be expressed by the following equation:

$$f(x, y) = \frac{1}{2\pi\sigma^2} \exp\left(-\frac{x^2 + y^2}{2\sigma^2}\right). \quad (19)$$

The  $Q(x, y)$  quantity is calculated by the summation of data:

$$Q(x, y) = \sum_{i,j} q(x_i, y_i) f(x - x_i, y - y_i) \quad (20)$$

where  $q(x_i, y_i)$  is a quantity at  $(x_i, y_i)$  before filtering. In other words,  $Q(x, y)$  is calculated using values around the position  $(x, y)$ . In our computations,  $\sigma$  was chosen to be the mesh size, which was the distance between the closest two data points. The mesh illustrated in Figs. 3 and 4 was  $120 \times 120$ . Some quantities, such as the stress tensor density and the kinetic energy density, calculated from the electronic structure by OpenMX, exhibit some noisy distribution when they are defined using the second derivative of wave functions or higher. Accordingly, the Gaussian filter was used for the comparison of our result, which was obtained employing the periodic boundary conditions, with the previously reported outcome [19].

## B. Hydrogen bond

Subsequently, the identification of the hydrogen bond was thoroughly investigated. In the previous subsection, we established that utilizing cluster models could be used to confirm the properties of ionic bonds. Consequently, the cluster models for the ionic bond were employed to discriminate the hydrogen bonds from the ionic ones. This is because, generally, computations based on molecular orbital methods using the cluster models are more accurate for the description of chemical bonds.

### 1. Eigenvalues of the stress tensor density at the Lagrange point

The Lagrange point has been previously used to characterize chemical bonds [17–19]. In the present study, in the first instance, the eigenvalue of the stress tensor density at the Lagrange point was studied.

TABLE II: The internuclear length, bond order of QED, and the eigenvalues of the stress tensor density at the Lagrange point.

	Internuclear length [ $\text{\AA}$ ]	$b_\epsilon$	$\tau_e^{S33}$ [a.u.]	$\tau_e^{S22}$ [a.u.]	$\tau_e^{S11}$ [a.u.]
(H <sub>2</sub> O) <sub>2</sub>	1.9946	0.0635	$1.2508 \times 10^{-3}$	$-1.0041 \times 10^{-2}$	$-1.0592 \times 10^{-2}$
(HF) <sub>2</sub>	1.9473	0.0609	$1.9195 \times 10^{-3}$	$-1.0254 \times 10^{-2}$	$-1.0254 \times 10^{-2}$
HF – H <sub>2</sub> O	1.7515	0.1351	$2.4795 \times 10^{-3}$	$-2.0849 \times 10^{-2}$	$-2.2867 \times 10^{-2}$
HF – NH <sub>3</sub>	1.7279	0.1839	$4.4115 \times 10^{-3}$	$-3.0268 \times 10^{-2}$	$-3.0268 \times 10^{-2}$
H <sub>2</sub> O – NH <sub>3</sub>	2.0212	0.0660	$7.6103 \times 10^{-4}$	$-1.0425 \times 10^{-2}$	$-1.0492 \times 10^{-2}$

For the six models demonstrated in Fig. 1, the Lagrange point of the hydrogen bond between two molecules was obtained for all molecules, with the exception of (NH<sub>3</sub>)<sub>2</sub>. The eigenvalue of the stress tensor density at the Lagrange point is shown in Table II. The internuclear length and the bond order of QED are also given. It is noteworthy that the internuclear length of the hydrogen bond is consistent with the previously reported typical length of a bond of this type. This confirms that except for the NH<sub>3</sub> homodimer, the models evaluated herein are valuable for studying hydrogen bonds. The bond order,  $b_\epsilon$ , of a hydrogen bond is significantly smaller than the bond order of a typical single bond of a covalent bond, which is approximately 1 [20]. The covalency of the hydrogen bond is weaker than that of a typical single covalent bond. Two eigenvalues,  $\tau_e^{S22}$  and  $\tau_e^{S11}$ , are exactly or nearly degenerate, since axial symmetry exists exactly or approximately around the axis of a hydrogen bond. The largest eigenvalue is positive for all bonds and this feature is in stark contrast to the metallic bond. Moreover, the value of the largest eigenvalue is much smaller than that of a covalent bond, and is comparable to the typical value of an ionic bond, i.e.,  $10^{-3} - 10^{-2}$  [19]. In this sense, a hydrogen bond can be easily distinguished from a metallic bond; however, it is difficult to distinguish it from ionic and weakly covalent bonds only in terms of the largest eigenvalue of the stress tensor density at the Lagrange point. This is attributed to the fact that the hydrogen bond exhibits ionicity and covalency. Furthermore, the typical length of a hydrogen bond is comparable to the typical length of an ionic bond.

In addition to the negative largest eigenvalue, metallic bonds are characterized by the degeneracy of eigenvalues at the Lagrange point. To see this property, the differential eigenvalues can be used for the discrimination of chemical bonds [17, 18]. Such analysis is also



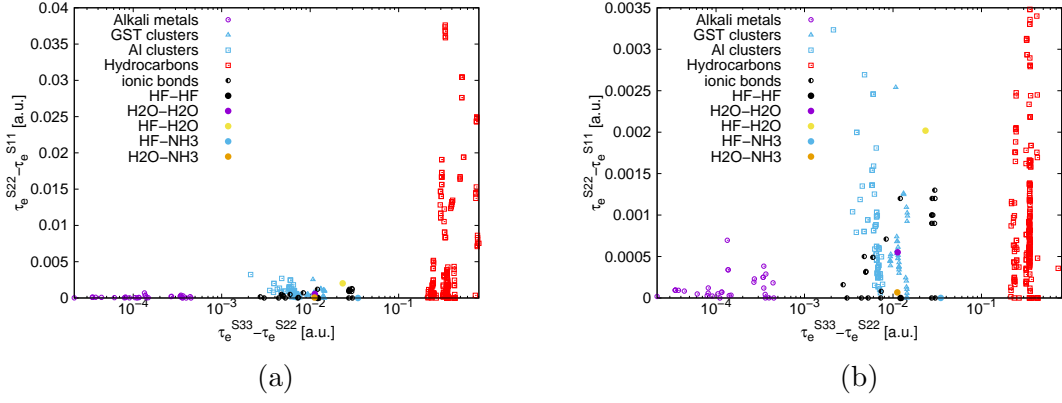


FIG. 5: The distribution of the differential eigenvalues of the electronic stress tensor density at the Lagrange point. Panel (b) is a magnified view of a part of panel (a). In both panels, the GST clusters indicate the previously reported data relating to the chemical bonds of the GeSbTe clusters [19].

useful for distinguishing metalloid bonds from metallic ones [18]. In Fig. 5, the differential eigenvalues of the electronic stress tensor density at the Lagrange point are shown as scatter plots of  $\tau_e^{S33} - \tau_e^{S22}$  and  $\tau_e^{S22} - \tau_e^{S11}$ . Other data, including hydrocarbons, alkali metal clusters, aluminum clusters, GeSbTe (GST) clusters, and ionic compound clusters evaluated in previous studies, are also presented [17–19]. Panel (b) is the magnified view of a part of panel (a). The previous works reveal that the differential eigenvalues of hydrocarbons are distributed in the rightmost part of the plots. Moreover, the largest eigenvalue of these molecules is significantly larger than the eigenvalues of the other molecules. This feature is a consequence of the directionality of covalent bonds. Furthermore, the values corresponding to alkali metals are accumulated in the bottom left corner, and the eigenvalues are strongly degenerate. Correspondingly, this observation is a result of the lack of directionality. The distribution of the values corresponding to metalloids (Al and GeSbTe) exhibits intermediate properties between alkali metals and hydrocarbon molecules, while the ionic bond displays a similar distribution to that of metalloids. Ionic bonds cannot be distinguished from metalloid bonds by only the eigenvalues. The eigenvalues of hydrogen bonds are also accumulated in this region. Thus, this type of bonds cannot be discriminated from ionic bonds or the bonds of metalloids based on the information shown in this the plots. Nevertheless, we determined that hydrogen bonds can be distinguished from metalloid bonds by the quantities at the Lagrange point.

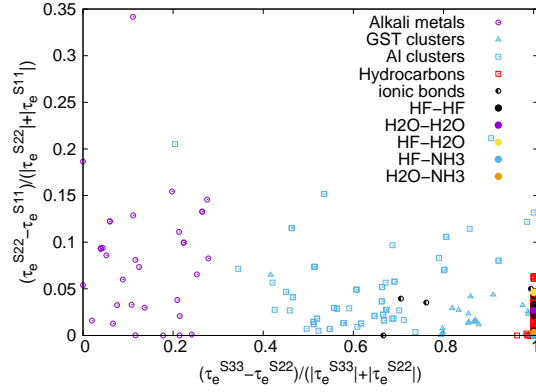


FIG. 6: The scatter plot showing the differential eigenvalues over the sum of the absolute value of the eigenvalues of the electronic stress tensor density at the Lagrange point.

Figure 6 illustrates the scatter plot of the differential eigenvalues over the sum of the absolute value of the eigenvalues of the electronic stress tensor density at the Lagrange point. The figure shows degeneracy free from the smallness of the magnitude of eigenvalues due to normalization. The normalized differential eigenvalues distinguish hydrogen bonds from the bonds of metalloids. Considering the normalized differential eigenvalues, with the exception of the ionic bonds, the distribution of the metalloid is separated from other bond types. Moreover, the distribution of the hydrogen bonds is analogous to that of the covalent bond. As shown in Table II, the eigenvalues of the hydrogen bonds are negligible, and the largest eigenvalue is considerably larger than other eigenvalues. Accordingly, based on the degeneracy of the eigenvalues of the stress tensor, it can be stated that hydrogen bonds exhibit directionality to the same extent as covalent bonds. In other words, from the viewpoint of field theoretical formalism, we confirmed that hydrogen bonds display features of weak covalent bonds. In addition, the smallness is understood through the smallness of the QED bond order. Metallic bonds and the bonds of metalloids can be easily discriminated from other types in Figs. 5 and 6; however, hydrogen bonds and some of the ionic ones cannot be distinguished.

## 2. Stress tensor density and kinetic energy density

Prior to the evaluation of the distributions of the stress tensor density and the kinetic energy density of hydrogen bonds, previously reported outcomes are summarized and explained

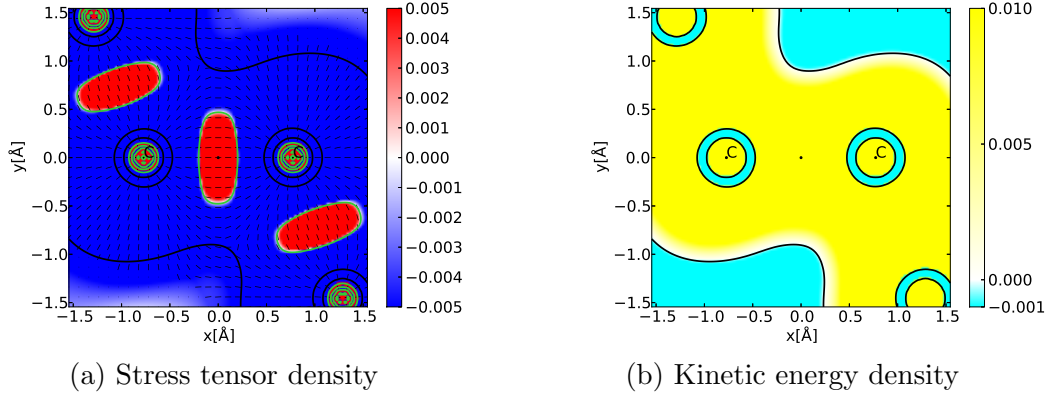


FIG. 7: The distributions of the stress tensor density and the kinetic energy density of covalent bonds between carbon atoms in a diamond cluster. Panel (a) illustrates the distribution of the largest eigenvalue of the stress tensor density and panel (b) shows the distribution of the kinetic energy density. Eigenvalues equal to zero are marked by green solid lines, while black line segments indicate the directions of the eigenvectors. In both panels, the black solid lines mark the electronic interface, where the kinetic energy density is zero. The Lagrange point is indicated by black dots.

in detail in Figs. 7, 8, and 9.

The stress tensor of covalent bonds were clarified in Ref. [16]. The distributions of the stress tensor density and the kinetic energy density of covalent bonds are shown in Fig. 7. Panel (a) illustrates the distribution of the largest eigenvalue of the stress tensor density and panel (b) demonstrates the distribution of the kinetic energy density. Eigenvalues equal to zero are marked by green solid lines, while black line segments indicate the directions of the eigenvectors. In both panels, the black solid lines mark the electronic interface, where the kinetic energy density is zero. Moreover, the Lagrange point is indicated by black dots. As it can be seen, the spindle structure is clearly present in the region between two carbon nuclei. Furthermore, the existence of the positive eigenvalue region around the Lagrange point is also noted. A bundle of eigenvectors connects the two nuclei in a shape of a rugby ball. In Fig. 7(b), the two carbon atoms are enveloped in the single electronic drop region, where the kinetic energy density is positive. Here, the separated electronic drop regions close to the nuclei represent the inner core electrons in the carbon atoms, i.e., the 1s electrons.

In Ref. [17], metallic bonds were studied in viewpoints of the stress tensor. In Fig. 8, the distributions of the stress tensor density and the kinetic energy density of the metallic bond are demonstrated analogously to the data shown in Fig. 7. We chose the bonds between

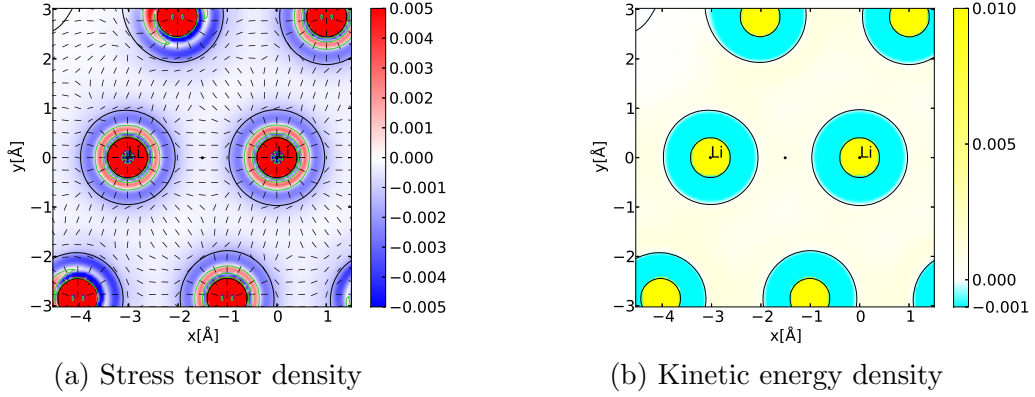


FIG. 8: The distributions of the stress tensor density and the kinetic energy density of the metallic bonds between lithium atoms in a lithium cluster. Both panels are depicted analogously to Fig. 7.

lithium atoms in a lithium cluster as the typical metallic bonds, mimicking a lithium crystal. As it can be seen in Fig. 8(a), no spindle structure can be found, and the largest eigenvalue of the metallic bond in the bond region, i.e. in the region between the two nuclei, is negative. In Fig. 8(b), the entire region is embedded in the single electronic drop region, with the exception of the arcs close to the nuclei. The separated circles represent the 1s core electrons in the lithium atoms.

Furthermore, Fig. 9 illustrates the distributions of the stress tensor density and the kinetic energy density of ionic bonds, which were reported in Ref. [19]. As discussed above, the discrimination from ionic bonds is crucial for the identification of hydrogen bonds, and two models, LiF and NaCl, were adopted for the study of typical ionic bonds. As seen from panels (b) and (d), all atoms exist in different electronic drop regions. The cations and anions are separated by the electronic atmosphere region and are bonded by electrostatic forces. Moreover, in panel (c), in NaCl, the largest eigenvalue at the Lagrange point is negative, while the distribution of eigenvectors connects the two nuclei in a spindle structure. Nonetheless, the eigenvectors are distributed radially from the nuclei; thus this is not a spindle structure. On the other hand, in panel (a), the pattern of the eigenvectors is nearly identical, while the largest eigenvalue at the Lagrange point is positive. Consequently, this may be misunderstood as a spindle structure. As discussed in the previously reported study [19], this positive eigenvalue corresponds to the outermost region of fluorine. Additionally, the positive region is not restricted to the direction of the lithium nucleus and the distribution of this region is nearly spherically symmetrical.

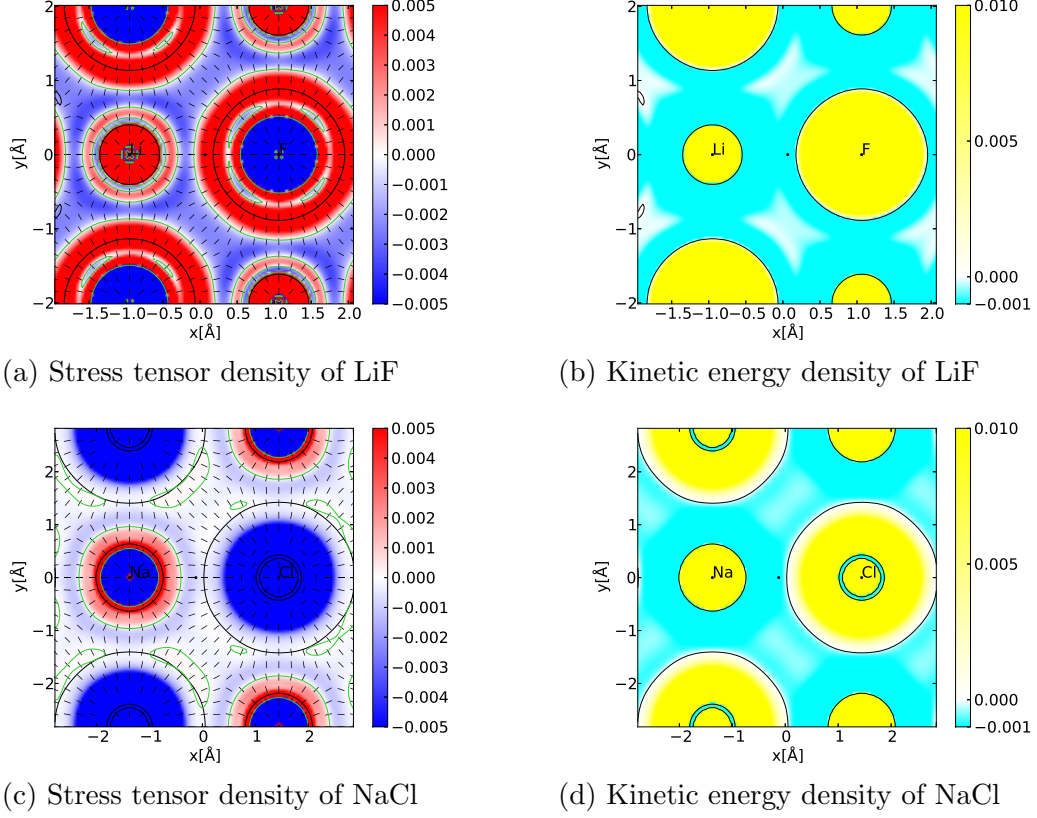
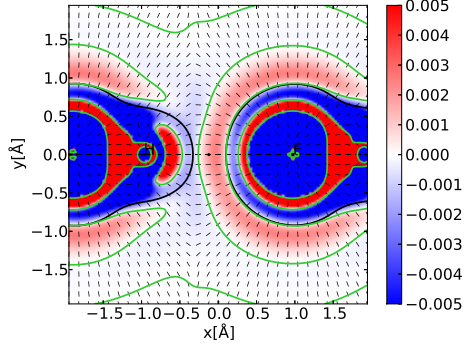
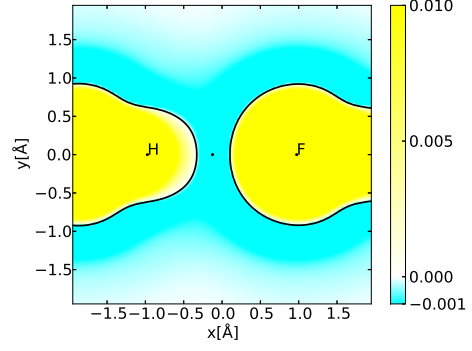


FIG. 9: The distributions of the stress tensor density and the kinetic energy density of the ionic bond. Two models were chosen as examples of ionic bonds. The top two panels illustrate the largest eigenvalue of the stress tensor density and the kinetic energy density of LiF, while the bottom images consider NaCl.

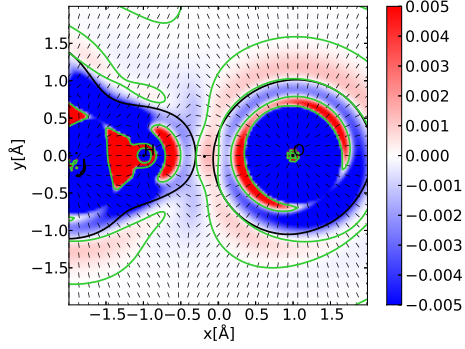
Figures 10 and 11 illustrate the distributions of the stress tensor density and the kinetic energy density of hydrogen bonds for homodimers and heterodimers, respectively. The results for  $(\text{HF})_2$ ,  $(\text{H}_2\text{O})_2$ , and  $(\text{NH}_3)_2$  are shown in Fig. 10, whereas the outcome for HF- $\text{H}_2\text{O}$ , HF- $\text{H}_2\text{O}$ , and  $\text{H}_2\text{O}$ - $\text{NH}_3$  are demonstrated in Fig. 11. With the exception of  $(\text{NH}_3)_2$ , the spindle structure, which characterizes covalent bonds, is clearly visible around the bond region between the hydrogen atoms and the acceptor atoms. The value of the largest eigenvalue of the stress tensor density at the Lagrange point is much smaller than that determined for a covalent bond. Moreover, the Lagrange point was not found in our  $(\text{NH}_3)_2$  model, which may be a consequence of the optimized structure. The positive eigenvalue regions around the hydrogen nucleus and in the vicinity of the surface of the nitrogen nucleus are distorted in the positive  $y$ -direction. As a result, N-H-N is significantly bent and is not considered



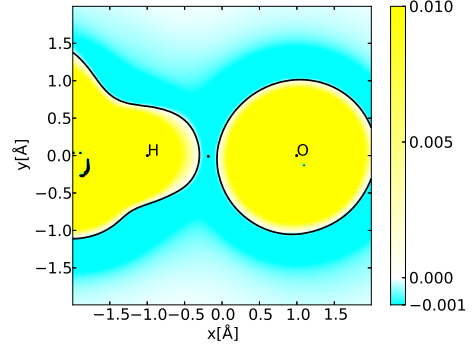
(a) Stress tensor density of (HF)<sub>2</sub>



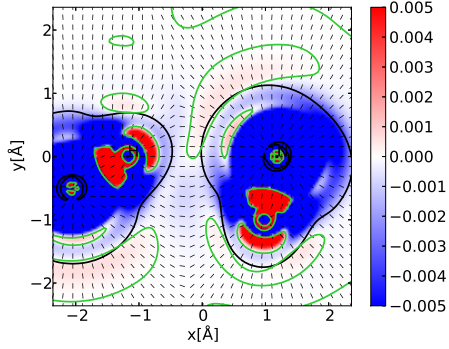
(b) Kinetic energy density of (HF)<sub>2</sub>



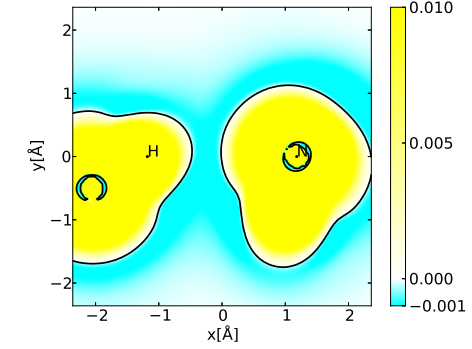
(a) Stress tensor density of (H<sub>2</sub>O)<sub>2</sub>



(b) Kinetic energy density of (H<sub>2</sub>O)<sub>2</sub>



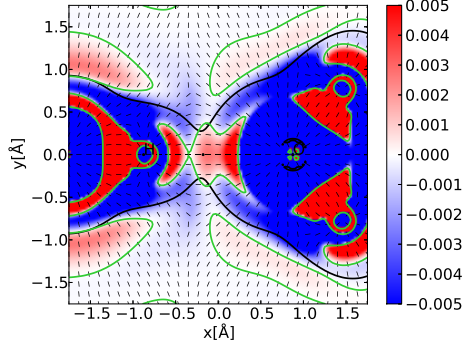
(a) Stress tensor density of (NH<sub>3</sub>)<sub>2</sub>



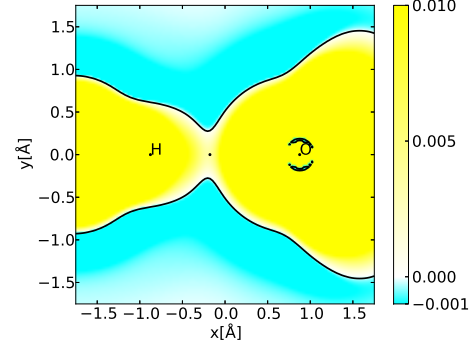
(b) Kinetic energy density of (NH<sub>3</sub>)<sub>2</sub>

FIG. 10: The distributions of the stress tensor density and the kinetic energy density of the hydrogen bond between two same molecules. (HF)<sub>2</sub>, (H<sub>2</sub>O)<sub>2</sub>, and (NH<sub>3</sub>)<sub>2</sub> are shown from top to bottom. The left and right columns demonstrates the largest eigenvalue of the stress tensor density and the kinetic energy density, respectively.

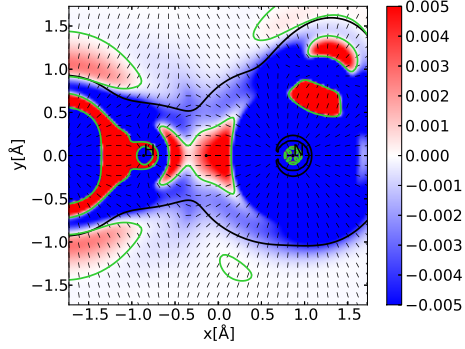
to be a typical hydrogen bond. The formation of this bond is not thoroughly understood and is beyond the scope of this work. (NH<sub>3</sub>)<sub>2</sub> was omitted in the subsequent investigations. For the hydrogen bonds of heterodimers, the positive eigenvalue region of the spindle structure is restricted to the direction between two nuclei. On the other hand, considering the



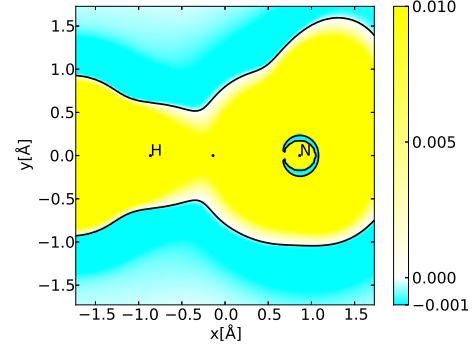
(a) Stress tensor density of HF-H<sub>2</sub>O



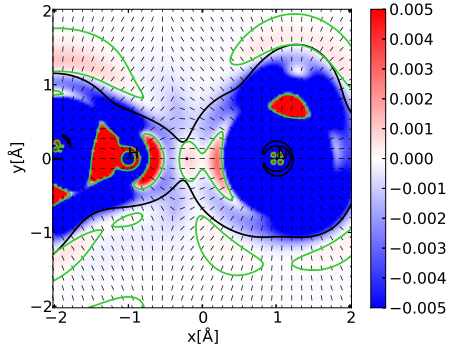
(b) Kinetic energy density of HF-H<sub>2</sub>O



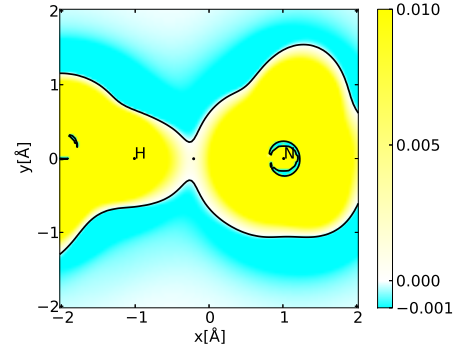
(a) Stress tensor density of HF-NH<sub>3</sub>



(b) Kinetic energy density of HF-NH<sub>3</sub>



(a) Stress tensor density of H<sub>2</sub>O-NH<sub>3</sub>



(b) Kinetic energy density of H<sub>2</sub>O-NH<sub>3</sub>

FIG. 11: The distributions of the stress tensor density and the kinetic energy density of hydrogen bonds between two different molecules. HF-H<sub>2</sub>O, HF-NH<sub>3</sub>, and H<sub>2</sub>O-NH<sub>3</sub> are shown from top to bottom. The left and right columns illustrates the largest eigenvalue of the stress tensor density and the kinetic energy density, respectively.

hydrogen bonds of homodimers, this region is distributed as a ring to cover the acceptor nuclei. This means that hydrogen bonds exhibit similarities to both the ionic and covalent bonds. Furthermore, the hydrogen bonds of heterodimers display stronger covalency than those of homodimers. Similar outcomes are also observed for the kinetic energy density. The



electronic drop regions around the donors and acceptors are clearly separated for the hydrogen bonds of homodimers, which is an obvious feature of ionic bonds. Conversely, for the hydrogen bond of heterodimers, the single electronic drop region includes both donors and acceptors. This region is narrowed, forming a bottleneck around the Lagrange point. Both the stress tensor density and the kinetic energy density results indicate that the ionicity of homodimer hydrogen bonds is stronger than that of heterodimer hydrogen bonds.

In summary, based on the conducted analysis, it can be concluded that hydrogen bonds exhibit features of both the covalent and ionic bonds. Moreover, a spindle structure is formed and the electronic drop regions are clearly separated for hydrogen bonds of homodimers. Nonetheless, it is challenging to distinguish hydrogen bonds from ionic bonds, particularly for ones of homodimers. Notably, as described above, the value of the largest eigenvalue at the Lagrange point can be utilized to discriminate hydrogen bonds from the covalent ones.

### 3. Directionality of the stress tensor

To allow more effective discrimination of the hydrogen bonds from the ionic ones, we subsequently investigated the directionality of the stress tensor. The directionality of hydrogen bonds is known to be considerably stronger than that of ionic bonds. Therefore, some directionality should be observed in the distribution of the stress tensor.

Figures 12, 13, and 14 illustrate the direction dependence of the largest eigenvalue of the stress tensor density of an ionic bond, a hydrogen bond of homodimers, and a hydrogen bond of heterodimers, respectively. In the figures, the horizontal axis,  $r$ , denotes the distance from the nucleus, and each line represents a different angle. Furthermore, in Figs. 9, 10, and 11, a zero degree angle for a nucleus indicates the direction to the other nucleus of a bond. The definition of the angle in these figures is clockwise. For the ionic bond, the largest eigenvalue of the stress tensor density is independent of the angle (all panels in Fig. 12). It is noteworthy that in panel (a), the values of  $\tau_e^{S33}$  are slightly different around  $r = 1.0$  [Å]. This outcome can be attributed to the difference in the contribution from the fluorine atom. The distribution of the stress tensor of a donor (acceptor) is not disturbed by an acceptor (donor). In other words, the ionic bond is isotropic around the nuclei. On the other hand, hydrogen bonds are dependent on the angle at approximately  $r = 0.2$  [Å], which is related to their directionality. All hydrogen bonds shown in Figs. 13 and 14 exhibit the same pattern



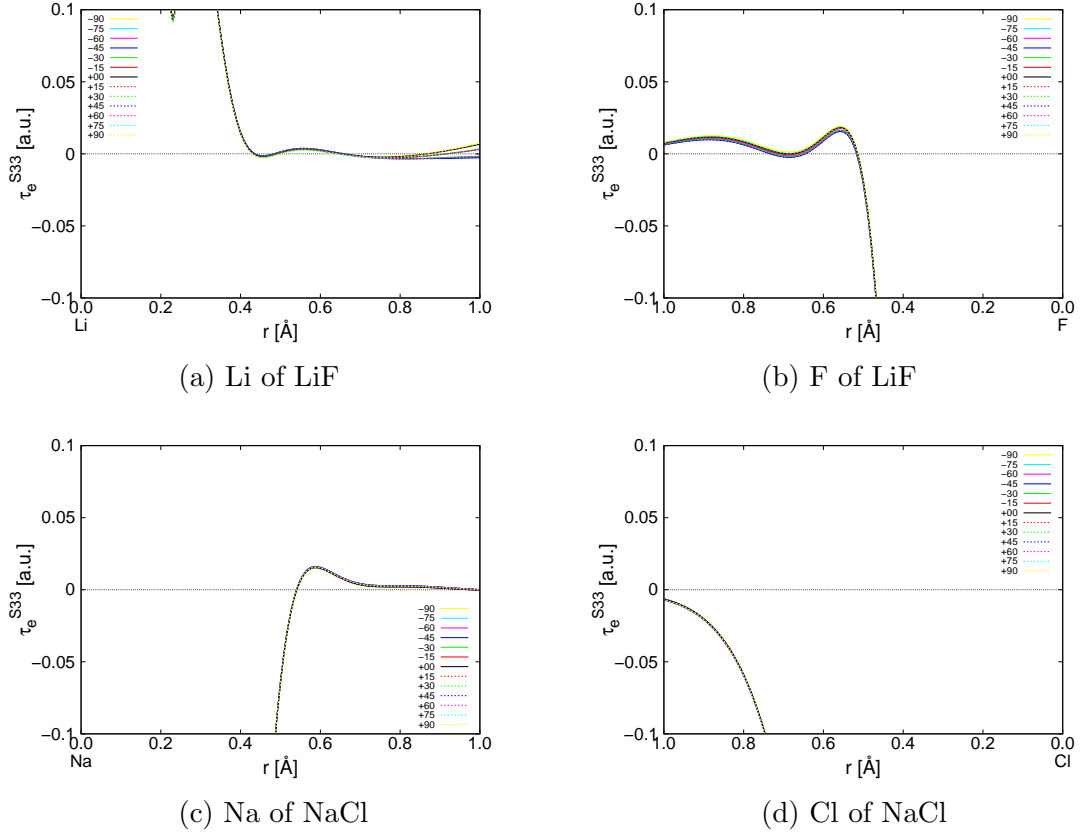


FIG. 12: The direction dependence of the largest eigenvalue of the stress tensor density of the ionic bond. Panels (a) and (b) illustrate the results around the Li and F atoms of LiF, respectively. Panels (c) and (d) show the results around the Na and Cl atoms of NaCl, respectively.

of the angle dependence around the hydrogen nuclei. Notably, the pattern is similar among the acceptors, though the similarity is less than in the case of hydrogen. This observation is attributed to the similarity of the electronic structure of the acceptor atoms, since in the present study, N, O, and F, which are located in the same row of the periodic table, were chosen as acceptors.

To parameterize this directionality quantitatively, we evaluated the values of the stress tensor at  $r = 0.2$  [Å] on the hydrogen side. This point was chosen, because the angle dependence of the eigenvalue for hydrogen bonds was determined to be maximum. The ratio of the largest eigenvalue of the stress tensor between  $0^\circ$  and  $45^\circ$  is shown in Table III. We adopted  $r = 0.2$  [Å] of hydrogen atoms for hydrogen bonds and Li and Na atoms for ionic ones, which are electron donor atoms. For typical ionic bonds, such as the ones in LiF and NaCl, the ratio is very close to 1, and the difference is negligible. On the other hand, the ratios for the hydrogen bonds are significantly larger, i.e.,  $1.16 - 1.47$ , due to

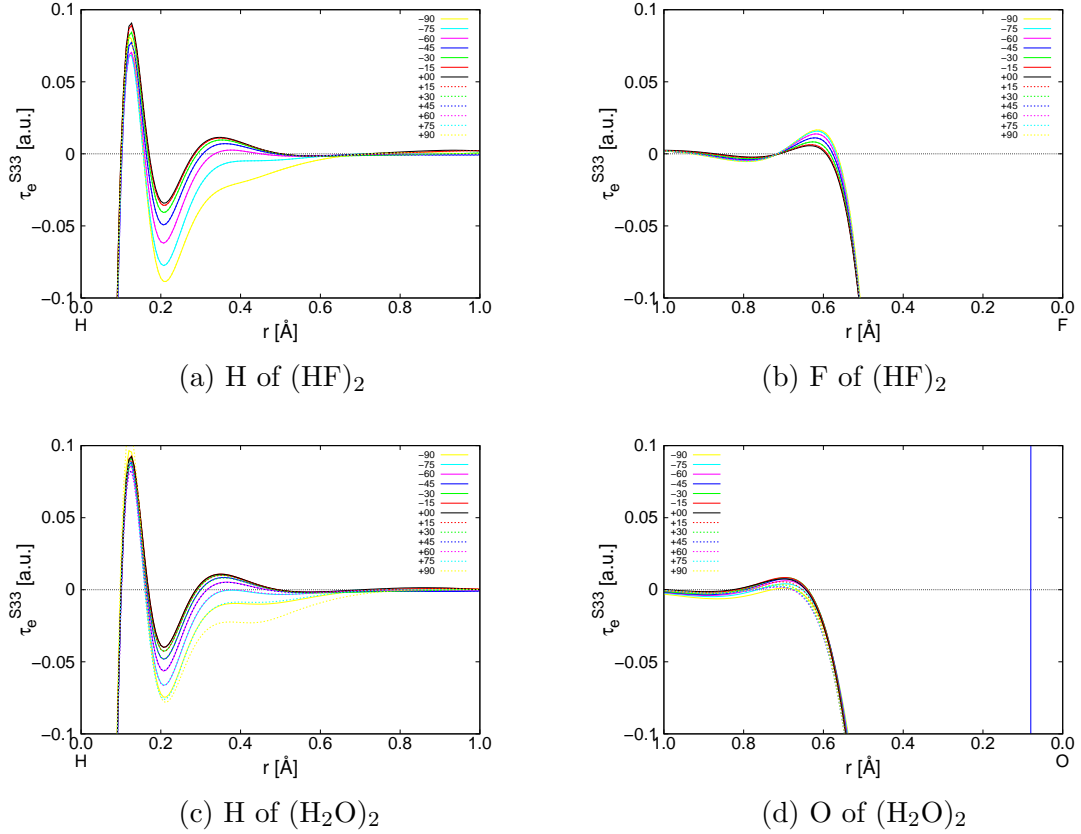


FIG. 13: The direction dependence of the largest eigenvalue of the stress tensor density of the hydrogen bonds of homodimers. Panels (a), (b), (c), and (d) show the results around the H and F atoms of  $(\text{HF})_2$  and around the H and O atoms of  $(\text{H}_2\text{O})_2$ , respectively.

the directionality. Complexes of homodimers show larger values of 1.42 and 1.47, while those of heterodimers exhibit smaller values of 1.16 – 1.37. We speculate that this trend is incidental, and further studies are necessary to clarify the reasons for our observation. Overall, hydrogen bonds could be distinguished from ionic bonds by the directionality of the largest eigenvalue of the stress tensor around the hydrogen nuclei. Importantly,  $r = 0.2$  [\AA] is only one example of values adopted in this work, which was considered to be appropriate in our models. Other values of  $r$  and additional criteria can also be employed, if they are able to extract the directionality of hydrogen bonds.

## V. SUMMARY

In the present study, hydrogen bonds were evaluated by QED in terms of the stress tensor density and the kinetic energy density. Identification of hydrogen bonds by QED was thor-

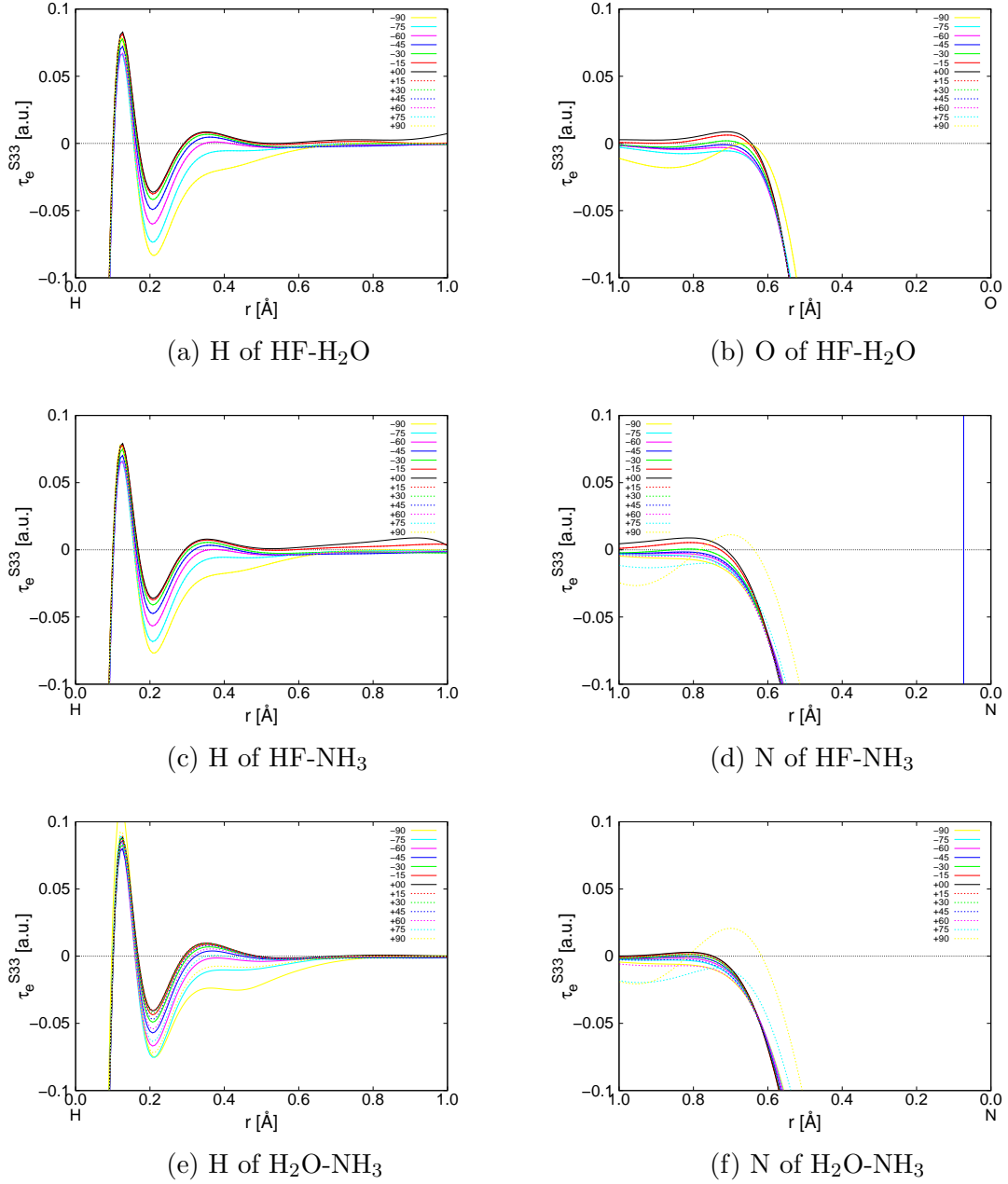


FIG. 14: The direction dependence of the largest eigenvalue of the stress tensor density of the hydrogen bonds of heterodimers. Panels (a), (b), (c), (d), (e), and (f) show the results around the H and O atoms of HF-H<sub>2</sub>O, around the H and N atoms of HF-NH<sub>3</sub>, and around the H and N atoms of H<sub>2</sub>O-NH<sub>3</sub>, respectively.

oughly discussed. It was determined that hydrogen bonds exhibit common features with ionic and covalent bonds. It was also established that the discrimination from the ionic bond is particularly important. We confirmed that the properties of ionic bonds, which had previously been determined by utilizing cluster models, are also observed in models with pe-

TABLE III: The ratio of the largest eigenvalue of the stress tensor between  $0^\circ$  and  $45^\circ$  at  $r = 0.2[\text{\AA}]$  from hydrogen atoms for hydrogen bonds and cation atoms for ionic bonds.

	nucleus	$\tau_{e0}^{S33}$ [a.u.]	$\tau_{e45}^{S33}$ [a.u.]	$\tau_{e45}^{S33}/\tau_{e0}^{S33}$
LiF	Li	$2.9885 \times 10^{-1}$	$2.9875 \times 10^{-1}$	0.9997
NaCl	Na	$-1.8225 \times 10^1$	$-1.8228 \times 10^1$	1.0002
(HF) <sub>2</sub>	H	$-3.2839 \times 10^{-2}$	$-4.8294 \times 10^{-2}$	1.4706
(H <sub>2</sub> O) <sub>2</sub>	H	$-3.8582 \times 10^{-2}$	$-5.4960 \times 10^{-2}$	1.4245
HF-H <sub>2</sub> O	H	$-3.4978 \times 10^{-2}$	$-4.8129 \times 10^{-2}$	1.3760
HF-NH <sub>3</sub>	H	$-3.4773 \times 10^{-2}$	$-4.6415 \times 10^{-2}$	1.3348
H <sub>2</sub> O-NH <sub>3</sub>	H	$-3.9402 \times 10^{-2}$	$-4.5764 \times 10^{-2}$	1.1615

periodic boundary conditions. We subsequently investigated the method for the identification of hydrogen bonds from other types of chemical bonds. Firstly, the metallic bonds could be discriminated by the degeneracy of eigenvalues of the stress tensor density at the Lagrange point. Eigenvalues of metallic bonds are very degenerate and the differences between them are less than  $10^{-3}$ . The difference between the two largest eigenvalues of hydrogen bonds was determined at approximately  $10^{-2}$ . Values of  $10^{-3}$  and  $10^{-2}$  are not considered to be dissimilar. If normalized differential eigenvalues were used, which involved the difference between two eigenvalues over the sum of the absolute values of the two eigenvalues, the values of the hydrogen bonds were approximately 1, while those of the metallic bonds were significantly lower. Hydrogen bonds also exhibit covalency, whereas the bond order of covalent bonds defined in QED is much less than the value of a typical covalent bond. The bond order of a hydrogen bond is typically between 0.06–0.18, while the value of a single covalent bond is approximately 1. This outcome arises from the difference in the values of the largest eigenvalue of the stress tensor density. Hydrogen bonds can be discriminated from covalent bonds by the comparison of the largest eigenvalue. The distinction from ionic bond is the most significant. Thus, in the current study, we paid particular attention to the directionality of hydrogen bonds. The distributions of the largest eigenvalues around the hydrogen atoms were found to vary. For the ionic bonds, the distribution was isotropic, while for the hydrogen bonds, it significantly depended on the angle from the internuclear axis. We demonstrated that the ratio of the eigenvalues between  $0^\circ$  and  $45^\circ$  at the point

distant from the hydrogen atom by 0.2 [Å] equals 1.2–1.5 for hydrogen bonds, while this ratio is 1 for ionic bonds. Analysis of chemical bonds by real space analyses based on quantum field theory, such as QED, was effectively conducted in the present study. Further work is necessary to clarify the nature of chemical bonds from the viewpoint of quantum field theory in more detail. Particularly, the bond order of metallic, ionic, and hydrogen bonds will be investigated in our future studies.

## Acknowledgments

This work was supported by a Grant-in-Aid for Scientific Research (C) (17K04982) and Grant for Basic Science Research Projects from The Sumitomo Foundation. The computations were performed in part using Research Center for Computational Science, Okazaki, Japan.

- 
- [1] P. de Silva and C. Corminboeuf, *J. Chem. Theory Comput.* 10, 3745 (2014).
  - [2] V. G. Tsirelson, A. I. Stash, I. V. Tokatly, *Mol. Phys.* 114, 1260, (2016).
  - [3] H. H. Osman, M. A. Salvadó, P. Pertierra, J. Engelkemier, D. C. Fredrickson, J. M. Recio, *J. Chem. Theory Comput.* 14, 104, (2018).
  - [4] R. F. W. Bader, *Atoms in Molecules: A Quantum Theory*, Oxford University Press, USA (1994).
  - [5] R. F. W. Bader, *J. Phys. Chem. A* 113, 10391 (2009).
  - [6] B. Silvi, A. Savin *Nature* 371, 683 (1994).
  - [7] F. Weinhold, *J. Comput. Chem.* 33, 2440 (2012).
  - [8] C. Foroutan-Nejad, S. Shahbazian, R. Marek, *Chem. Eur. J.* 20, 10140 (2014).
  - [9] C. Lepetit, P. Fau, K. Fajerweg, M. L. Kahn, B. Silvi, *Coord. Chem. Rev.* 345, 150 (2017).
  - [10] F. Fuster, S. J. J. Grabowski, *J. Phys. Chem. A* 115, 10078 (2011).
  - [11] For example, see, A. Tachibana, *New Aspects of Quantum Electrodynamics* (Springer, 2017).
  - [12] A. Tachibana, *J. Chem. Phys.* 115, 3497 (2001).
  - [13] A. Tachibana, Field Energy Density In Chemical Reaction Systems. In *Fundamental World of Quantum Chemistry, A Tribute to the Memory of Per-Olov Löwdin*, E. J. Brändas and

- E. S. Kryachko Eds., Kluwer Academic Publishers, Dordrecht (2003), Vol. II, pp 211-239.
- [14] A. Tachibana, J. Mol. Model. 11, 301 (2005).
  - [15] A. Tachibana, J. Mol. Struct. (THEOCHEM), 943, 138 (2010).
  - [16] P. Szarek and A. Tachibana, J. Mol. Model. 13, 651 (2007).
  - [17] K. Ichikawa, H. Nozaki, N. Komazawa, A. Tachibana, AIP ADVANCES 2, 042195 (2012).
  - [18] H. Nozaki, Y. Ikeda, K. Ichikawa, A. Tachibana, J. Comput. Chem. 36, 1240 (2015).
  - [19] H. Nozaki, Y. Fujii, K. Ichikawa, T. Watanabe, Y. Aihara, A. Tachibana, J. Comput. Chem. 37, 1924 (2016).
  - [20] P. Szarek, Y. Sueda, and A. Tachibana, J. Chem. Phys. 129, 094102 (2008).
  - [21] For a review see, S. J. Grabowski, Chem. Rev. 111, 2597 (2011), and references therein.
  - [22] A. Tachibana, Electronic Stress with Spin Vorticity. In *Concepts and Methods in Modern Theoretical Chemistry*, S. K. Ghosh and P. K. Chattaraj Eds., CRC Press, Florida (2013), pp 235-251.
  - [23] A. Tachibana, J. Comput. Chem. Jpn. 13, 18 (2014).
  - [24] S. T. Epstein, J. Chem. Phys. 63, 3573 (1975).
  - [25] A. M. Pendás, J. Hernández-Trujillo, J. Chem. Phys. 137, 134101 (2012); J. Maza, S. Jenkins, S. R. Kirk, J. S. M. Anderson, P. W. Ayers, Phys. Chem. Phys. Chem. 15, 17823 (2013).
  - [26] H. Nozaki, M. Senami, K. Ichikawa, A. Tachibana, Jpn. J. Appl. Phys. 55, 08PE01 (2016).
  - [27] M. Senami, Y. Ikeda, A. Fukushima, and A. Tachibana, Jpn. J. Appl. Phys. 49, 115002 (2010).
  - [28] A. Tachibana, Int. J. Quantum Chem. 100, 981 (2004).
  - [29] T. Ozaki *et al.*, OpenMX package, <http://www.openmx-square.org/>.
  - [30] T. Ozaki, Phys. Rev. B 67, 155108, (2003); T. Ozaki and H. Kino, Phys. Rev. B 69, 195113 (2004); T. Ozaki and H. Kino, Phys. Rev. B 72, 045121 (2005); K. Lejaeghere *et al.*, Science 351, aad3000 (2016).
  - [31] D. M. Ceperley and B. J. Alder, Phys. Rev. Lett. 45, 566(1980); J. P. Perdew and A. Zunger, Phys. Rev. B 23, 5048 (1981).
  - [32] *QEDynamics*, M. Senami, K. Ichikawa, A. Tachibana (<https://github.com/mfukudaQED/QEDalpha>)
  - [33] Gaussian 09, Revision E.01, M. J. Frisch, G. W. Trucks, H. B. Schlegel, G. E. Scuseria, M. A. Robb, J. R. Cheeseman, G. Scalmani, V. Barone, B. Mennucci, G. A. Petersson, H. Nakatsuji, M. Caricato, X. Li, H. P. Hratchian, A. F. Izmaylov, J. Bloino, G. Zheng, J. L. Sonnenberg,

M. Hada, M. Ehara, K. Toyota, R. Fukuda, J. Hasegawa, M. Ishida, T. Nakajima, Y. Honda, O. Kitao, H. Nakai, T. Vreven, J. A. Montgomery, Jr., J. E. Peralta, F. Ogliaro, M. Bearpark, J. J. Heyd, E. Brothers, K. N. Kudin, V. N. Staroverov, T. Keith, R. Kobayashi, J. Normand, K. Raghavachari, A. Rendell, J. C. Burant, S. S. Iyengar, J. Tomasi, M. Cossi, N. Rega, J. M. Millam, M. Klene, J. E. Knox, J. B. Cross, V. Bakken, C. Adamo, J. Jaramillo, R. Gomperts, R. E. Stratmann, O. Yazyev, A. J. Austin, R. Cammi, C. Pomelli, J. W. Ochterski, R. L. Martin, K. Morokuma, V. G. Zakrzewski, G. A. Voth, P. Salvador, J. J. Dannenberg, S. Dapprich, A. D. Daniels, O. Farkas, J. B. Foresman, J. V. Ortiz, J. Cioslowski, and D. J. Fox, Gaussian, Inc., Wallingford CT, 2013.

[34] R. A. Kendall, T. H. Dunning Jr., and R. J. Harrison, *J. Chem. Phys.* 96, 6796 (1992).